Calcium-activated nonspecific cation current and synaptic depression promote network-dependent burst oscillations

Jonathan E. Rubin[a,1], **John A. Hayes**[b,c,1], **Jeffrey L. Mendenhall**[b], **and Christopher A. Del Negro**[b,2]

[a]Department of Mathematics, 301 Thackeray Hall, University of Pittsburgh, Pittsburgh, PA 15260; [b]Department of Applied Science, 318 McGlothlin-Street Hall, The College of William and Mary, Williamsburg, VA 23187-8795; and [c]Department of Biology, Integrated Science Center 1, The College of William and Mary, Williamsburg, VA 23187-8795

Edited by Nancy J. Kopell, Boston University, Boston, MA, and approved December 24, 2008 (received for review September 6, 2008)

Central pattern generators (CPGs) produce neural-motor rhythms that often depend on specialized cellular or synaptic properties such as pacemaker neurons or alternating phases of synaptic inhibition. Motivated by experimental evidence suggesting that activity in the mammalian respiratory CPG, the preBötzinger complex, does not require either of these components, we present and analyze a mathematical model demonstrating an unconventional mechanism of rhythm generation in which glutamatergic synapses and the short-term depression of excitatory transmission play key rhythmogenic roles. Recurrent synaptic excitation triggers postsynaptic Ca^{2+}-activated nonspecific cation current (I_{CAN}) to initiate a network-wide burst. Robust depolarization due to I_{CAN} also causes voltage-dependent spike inactivation, which diminishes recurrent excitation and thus attenuates postsynaptic Ca^{2+} accumulation. Consequently, activity-dependent outward currents—produced by Na/K ATPase pumps or other ionic mechanisms—can terminate the burst and cause a transient quiescent state in the network. The recovery of sporadic spiking activity rekindles excitatory interactions and initiates a new cycle. Because synaptic inputs gate postsynaptic burst-generating conductances, this rhythm-generating mechanism represents a new paradigm that can be dubbed a 'group pacemaker' in which the basic rhythmogenic unit encompasses a fully interdependent ensemble of synaptic and intrinsic components. This conceptual framework should be considered as an alternative to traditional models when analyzing CPGs for which mechanistic details have not yet been elucidated.

breathing | burst mechanism | central pattern generator

Central pattern generator networks produce neural rhythms that drive motor behaviors (1, 2). Many CPGs function in reduced preparations in vitro, which facilitates studies at the cellular and synaptic levels. Building blocks such as bursting-pacemaker neurons and reciprocal synaptic inhibition often form the core of the rhythmogenic mechanism (3). However, the CPG for inspiratory breathing movements in mammals, the preBötzinger Complex (preBötC) (4, 5), exhibits rhythmicity after removal of synaptic inhibition (6, 7) and after blockade of bursting-pacemaker activity in individual neurons (8, 9).

A group pacemaker has been proposed as the building block of an alternative paradigm for respiratory rhythmogenesis (10). The group pacemaker concept refers to a network that employs recurrent synaptic excitation to boost and spread activity like a conventional network oscillator (3), yet generates bursting oscillations in which cells show a plateau depolarization—or drive potential—during the active phase, as typically associated with intrinsic pacemaker properties. Until recently, the group pacemaker model has remained purely heuristic and hypothetical, without an explicit mathematical instantiation or mechanistic connection to experimental findings.

We tested the viability of an experimentally motivated group pacemaker model, where neurons express a Ca^{2+}-activated nonspecific monovalent cation current (I_{CAN}) with its activation linked to group I metabotropic glutamate receptors (mGluRs) and AMPA receptors that, together, increase intracellular Ca^{2+} (11). I_{CAN} is normally latent, but this synaptically triggered Ca^{2+} flux evokes I_{CAN}, which underlies the burst phase of network activity (12, 13). I_{CAN} may be well suited to play a central role in a group pacemaker because it contributes to plateau depolarizations in diverse contexts such as spinal locomotor networks (14), autonomic motor systems (15), subthalamic neurons (16), and the entorhinal cortex (17), among others.

Our model shows how recurrent excitation and I_{CAN} generate a burst and, further, predicts that I_{CAN} hastens burst termination by causing voltage-dependent spike inactivation. The attenuation of spikes diminishes recurrent excitation, yielding a form of synaptic depression that deactivates I_{CAN}. This deactivation in turn allows activity-dependent outward currents to interrupt spiking and establish a quiescent phase. The eventual resumption of spontaneous spiking restarts recurrent positive feedback and initiates a new cycle, leading to systematic burst oscillations of the network.

With synaptic signals gating burst-generating ion channels in postsynaptic neurons, the group pacemaker model provides a new paradigm for CPG activity in which the rhythmogenic unit is the ensemble of coupled synaptic and intrinsic membrane properties. Physiological studies of respiratory rhythmogenesis guided the model formulation, yet it incorporates general elements that are found across a variety of brain areas. CPGs are ubiquitous throughout the animal kingdom and the rhythmogenic mechanisms are often incompletely understood. Given its relevance to the preBötC and the tendency for successful mechanisms to be harnessed across brain regions and among diverse species, the group pacemaker model presents a viable alternative to bursting-pacemaker neurons, reciprocal inhibition, or conventional network oscillations as the basis for network-level rhythmogenesis.

Results

Model neurons with Hodgkin-Huxley-style spike-generating and leak currents, and I_{CAN}, were mutually coupled via ionotropic AMPA receptors and group I mGluRs, which elevated intracellular Ca^{2+} to activate I_{CAN} (Fig. S1). We set intrinsic properties such that, in the absence of coupling, one neuron (N_2) was quiescent and the other (N_1) spiked tonically (Fig. 1*A*). Nevertheless, both neurons

---

Author contributions: J.E.R., J.A.H., and C.A.D.N. designed research; J.E.R., J.A.H., and C.A.D.N. performed research; J.A.H. and J.L.M. contributed new reagents/analytic tools; J.E.R., J.A.H., and C.A.D.N. analyzed data; and J.E.R., J.A.H., and C.A.D.N. wrote the paper.

The authors declare no conflict of interest.

This article is a PNAS Direct Submission.

[1]J.E.R. and J.A.H. contributed equally to this work.

[2]To whom correspondence should be addressed. E-mail: cadeln@wm.edu.

This article contains supporting information online at www.pnas.org/cgi/content/full/0808776106/DCSupplemental.

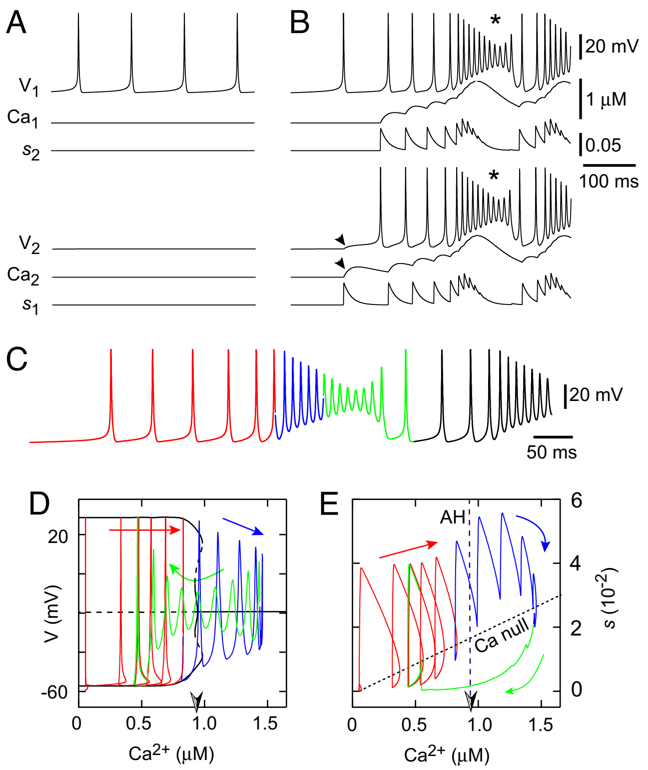

Fig. 1. Group pacemaker models. (*A* and *B*) Uncoupled (*A*) and coupled (*B*) model neurons, showing voltage (V), Ca^{2+}, and synaptic dynamics (s). Neuron 1 (N$_1$, top) is initially tonic (*A*) and Neuron 2 (N$_2$, bottom) is initially quiescent (*A*), before coupling (*B*). (*C*) Self-coupled single neuron with dynamics that resemble the 2-neuron case. Color coding applies to phase-plane analyses in D and E. (*D*) V-Ca^{2+} bifurcation diagram (black) with solution trajectory. Solid (dashed) black curves denote stable (unstable) structures, which are either nodes or the maximal and minimal voltages along families of periodic orbits. These include a curve of steady states at approximately -20 mV, which switches from unstable to stable in a supercritical Andronov-Hopf bifurcation (AH, half-shaded arrowhead; $(\mathrm{Ca}^{2+})_{\mathrm{AH}}$ in text) as Ca^{2+} increases, and 3 families of periodic orbits, a stable one that emerges from the AH bifurcation, an unstable family that emerges from the first, and a second stable family of larger amplitude (in maximal and minimal voltage) that emerges from the unstable periodic orbits. Red, blue, and green portions correspond to the voltage trace in C. Voltage spikes follow the large amplitude periodic orbits. Spike attenuation begins when Ca^{2+} becomes so large that this family of periodic orbits no longer exists. Because this occurs very close to $(\mathrm{Ca}^{2+})_{\mathrm{AH}}$, we approximate the point where spike attenuation begins by $(\mathrm{Ca}^{2+})_{\mathrm{AH}}$ for simplicity (see text). (*E*) The *s*-Ca^{2+} phase plane showing the curve of AH points (the half-shaded arrowhead denotes $(\mathrm{Ca}^{2+})_{\mathrm{AH}}$), and the Ca^{2+} nullcline (Ca null), with the solution trajectory in red, blue, and green.

had low Ca^{2+} concentrations in the absence of coupling (Ca$_1$ and Ca$_2$ $\approx$ 50 nM).

A synaptic connection enabled N$_1$ to excite N$_2$. Spikes in N$_1$ that initially peaked at 30 mV crossed the synaptic threshold θ_s and incremented the synaptic variable s_1. The increase in s_1 depolarized N$_2$ via AMPA receptors and caused Ca$_2$ to increase (Fig. 1*B*, arrowheads). The rise in Ca$_2$ evoked I_{CAN} and N$_2$ commenced spiking. Recruiting the quiescent cell boosted the synaptic variable s_2, which depolarized N$_1$,elevated Ca$_1$, and activated I_{CAN} in N$_1$. The positive feedback loop of Ca^{2+} elevation and I_{CAN} recruitment produced mutual depolarization of $\approx$30 mV with a superimposed burst of spiking at $\approx$100 Hz, even though neither neuron produced bursts or high frequency spiking in the absence of coupling.

After a period of rapid spiking, depolarization block subsequently reduced spike amplitudes (Fig. 1*B*, asterisks). Because V$_1$ and V$_2$ failed to reach θ_s, s_1 and s_2 stopped growing and intracellular Ca^{2+} stopped accumulating. Extrusion and sequestration then dominated the Ca^{2+} dynamics and Ca$_1$ and Ca$_2$ declined, deactivating I_{CAN}. After this decline and associated relief of depolarization block, the cells resumed tonic spiking, which quickly ramped up in frequency through reciprocal synaptic excitation, such that the cycle repeated with no significant pauses between bursts (Fig. 1*B*).

We analyzed how Ca^{2+} and synaptic dynamics govern bursting behavior in the model by computing a bifurcation diagram for a single cell that was tonically active in isolation but, when self-coupled, displayed burst-like oscillations (Fig. 1*C*) that resemble the 2-cell case (Fig. 1*B*). We determined the voltage and synaptic dynamics for fixed Ca^{2+} within a range of physiological values, because the rate of change of Ca^{2+} is small compared with voltage and *s*. The resulting diagram shows that for each sufficiently low level of Ca^{2+}, the stable feature is a periodic orbit, corresponding to large-amplitude spiking. As Ca^{2+} increases to a critical value $(\mathrm{Ca}^{2+})_{\mathrm{AH}}$, a supercritical Andronov-Hopf (AH) bifurcation occurs, beyond which the only stable state corresponds to depolarization block (Fig. 1*D*).

Fig. 1*D* superimposes the voltage and Ca^{2+} components of the solution trajectory onto the bifurcation diagram. Because the periodic orbit amplitudes remain relatively constant (red) until very close to the AH bifurcation, spike attenuation does not begin until Ca^{2+} reaches $(\mathrm{Ca}^{2+})_{\mathrm{AH}}$ (red-blue). Spike amplitudes do not decrease rapidly when Ca^{2+} exceeds $(\mathrm{Ca}^{2+})_{\mathrm{AH}}$ (blue-green) because the depolarization block steady state is weakly attracting, i.e., linearization about this stable state yields eigenvalues with negative real parts of small magnitude.

The curve in state space at which the rate of change of Ca^{2+} switches signs is called the Ca^{2+} nullcline and is naturally visualized in the *s*-Ca^{2+} phase plane because Ca^{2+} changes are synaptically driven (11). During spiking, *s* and Ca^{2+} increase (Fig. 1*E*, red). Ca^{2+} eventually exceeds $(\mathrm{Ca}^{2+})_{\mathrm{AH}}$, and spikes diminish (blue). Voltage is not visible in the *s*-Ca^{2+} plane, but because Fig. 1 *D* and *E* share the same Ca^{2+} axis, the voltage in Fig. 1*E* can be deduced from Fig. 1*D* based on whether Ca^{2+} is increasing or decreasing along the bifurcation diagram. The Ca^{2+} nullcline is crossed in the downward direction when attenuated spikes no longer boost *s*. Intracellular Ca^{2+} levels drop (Fig. 1*E*, green) until Ca^{2+} recrosses $(\mathrm{Ca}^{2+})_{\mathrm{AH}}$ and spikes grow to approach the stable large amplitude orbits present for $\mathrm{Ca}^{2+} < (\mathrm{Ca}^{2+})_{\mathrm{AH}}$. The reemergence of full-amplitude spikes drives increases in *s*, causing the Ca^{2+} nullcline to be crossed in the upward direction and allowing Ca^{2+} to increase again. The resulting Ca^{2+} elevation reactivates I_{CAN} and the burst cycle repeats (Fig. 1 *D* and *E*, green-red).

The mechanism described above leads to periodic waxing and waning of spike activity but does not produce extended quiescent periods between bursts (Fig. 2*A*). Indeed, the branch of periodic orbits born at $(\mathrm{Ca}^{2+})_{\mathrm{AH}}$ enables repetitive overshooting spikes that do not depend on I_{CAN} and persist for all $\mathrm{Ca}^{2+} < (\mathrm{Ca}^{2+})_{\mathrm{AH}}$ (Fig. 1*D*). Periods of quiescence that are characteristic of CPG rhythms require the existence of a branch of stable resting states in the bifurcation diagram. Lowering E_{L} below -60 mV (Fig. 2*B*) enhanced the K$^+$-dominated leak current (I_{Leak}) and created a branch of stable nodes, at resting potentials akin to V$_2$ in Fig. 1*A*, and a branch of saddle points seen at $\mathrm{Ca}^{2+} < (\mathrm{Ca}^{2+})_{\mathrm{AH}}$ in the V-Ca^{2+} bifurcation diagram (Fig. 2*D*). Because I_{Leak} is not dynamic, once the voltage settled onto the stable branch it could not leave, regardless of the strength of self-coupling (Fig. 2*B*). Adding Gaussian noise to the current-balance equation (see *SI Appendix*) enabled the system to move spontaneously between the active and quiescent phases. Noise-driven spikes randomly occurring in succession could trigger bursts (Fig. 2*C*), which evolved with the same dynamics as Fig. 1*C*. However, with lower E_{L} and noise fluctuations, the system could spontaneously jump back to the quiescent state when Ca^{2+} was near its nadir, terminating the burst. The dependence of burst termination on noise fluctuations also allowed for back-to-back bursts (Fig. 2*C Inset*) before burst termination and yielded irregular

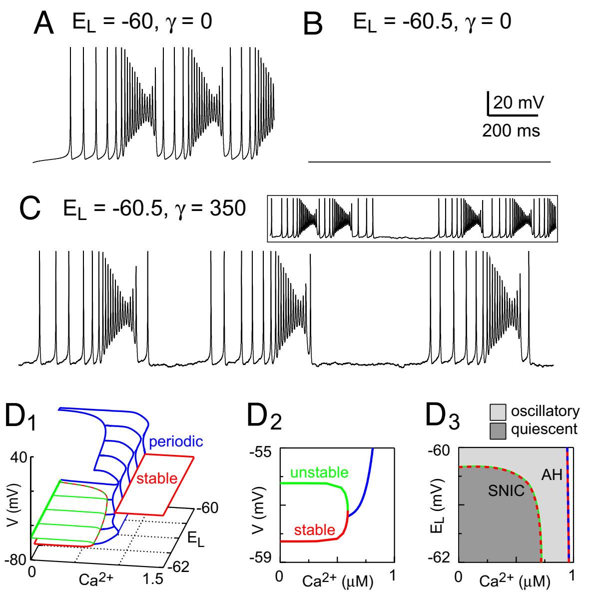

Fig. 2. Noise-induced burst oscillations in the self-coupled model. (*A*) Oscillations and (*B*) quiescence depend on E_L with no added noise. (*C*) The addition of membrane noise ($\gamma = 350$ pA^2) allows irregular bursting for low E_L. (*Inset*) Back-to-back bursts in this regime. (D_1) Three-dimensional (3D) bifurcation diagram with Ca^{2+} and E_L as bifurcation parameters. The red and green surfaces consist of stable nodes and saddle points, respectively; the blue surface is formed from the maximum and minimum voltages along families of periodic orbits. (D_2) V-Ca^{2+} slice of the 3D graph in D_1 with $E_L = -60.5$ mV showing the lower stable node branch, the branch of saddle points (which reflect spike threshold), and the minimum voltage from the family of periodic orbits that coalesce in a SNIC bifurcation. (D_3) E_L-Ca^{2+} plane showing the curve of SNIC bifurcation points and the curve of Andronov-Hopf (AH) bifurcation points from which the periodic orbit families emanate, extracted from the 3D graph in D_1. Dark and light gray regions correspond, respectively, to quiescent and oscillatory solutions in the self-coupled model with Ca^{2+} held constant.

burst sequences that changed phase erratically, lacking the regularity of CPG-driven rhythmic behaviors.

To engender a rhythm with regular quiescent interburst intervals, we added an outward current, I_{pump}, due to electrogenic Na/K ATPase pumps (Fig. S1) that activate in response to Na$^+$ accumulation during the I_{CAN}-dominated inspiratory burst (18–21). With low initial Na$^+$ levels and I_{pump} deactivated, the self-coupled cell spiked at a low frequency (Fig. 3, red). As shown previously, recurrent excitation and I_{CAN} activation transformed this activity into a high frequency burst of spikes. Ca^{2+} continued to increase and the trajectory moved rightward in the V-Ca^{2+} bifurcation diagram, yielding a phase of spike attenuation as Ca^{2+} exceeded (Ca^{2+})$_{\mathrm{AH}}$. These burst dynamics, shown in Fig. 3*B*, appear similar to Fig. 1*D*. However, with sufficient Na$^+$ accumulation and corresponding I_{pump} activation, the family of periodic orbits born at (Ca^{2+})$_{\mathrm{AH}}$ terminated at a level of Ca^{2+} below (Ca^{2+})$_{\mathrm{AH}}$, where the periodic family coalesced with a new branch of stable nodes near −60 mV (Fig. 3*Bb*). The emergence of these stable nodes and the corresponding unstable saddle points is illustrated in Fig. 3*C*, which superimposes the V-Ca^{2+} bifurcation structures from Fig. 3*B*. The periodic family in the low Na$^+$ case (curve a) does not terminate at any Ca^{2+} < (Ca^{2+})$_{\mathrm{AH}}$. However, because Na$^+$ accumulates and I_{pump} activates, the stable branch appears and expands to occupy a greater proportion of the Ca^{2+} space (curves b and c). This I_{pump}-related branch is analogous to that created by lowering E_L in Fig. 2*D*. The periodic orbits and stable nodes meet at a saddle-node on an invariant circle (SNIC) bifurcation in the V-Ca^{2+} diagram, and we define the corresponding Ca^{2+} level as (Ca^{2+})$_{\mathrm{SNIC}}$ (Figs. 2D_3 and 3*D*).

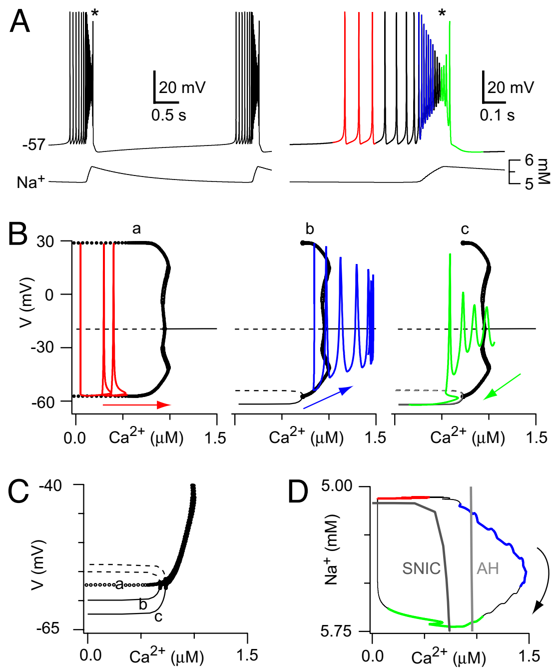

Fig. 3. Self-coupled model with I_{pump}. (*A*) Voltage and Na$^+$ traces (*Left*) with an expanded and color-coded burst (*Right*). (*B*) V-Ca^{2+} bifurcation diagrams for fixed Na$^+$ values; red, blue, and green trajectories correspond to A. Stable (unstable) points are drawn with solid (dashed) lines, and periodic orbits (maximal and minimal voltages) are shown with circles. The branch near −20 mV is a curve of spiral points, featuring a change in stability at the AH bifurcation from which the periodic orbits emanate. The branches at lower voltages that appear in the *Center* (*b*) and *Right* (*c*) parts of *B*, consist of unstable saddles (dashed lines) and stable nodes (solid lines), which intersect at a SNIC bifurcation. (*C*) Expanded view near the SNIC; a, b, and c refer to *Left* (*a*), *Center* (*b*), and *Right* (*c*) in *B*, superimposed without trajectories. (*D*) The burst cycle in Na$^+$-Ca^{2+} state space, together with the SNIC and AH curves. Na$^+$ is plotted such that lower values on the *y* axis reflect lower excitability, due to higher Na$^+$ evoking greater I_{pump} (outward) current.

When the stable branch first appeared, it was not visited by the trajectory (Fig. 3*Bb*). Depolarization block and subsequent synaptic depression led to a drop in Ca^{2+} and changed the direction of the trajectory along the Ca^{2+} axis (Fig. 3*Bc*). Even as Ca^{2+} declined from its peak value (1.5 μM), Ca^{2+} levels were high enough to maintain sufficient I_{CAN} activation so that Na$^+$ continued accumulating. Therefore, I_{pump} continued to strengthen, expanding the stable branch of quiescent states until the trajectory, moving leftward relative to the V-Ca^{2+} bifurcation diagram, crossed the SNIC bifurcation and the quiescent state became globally attracting, yielding burst termination (Fig. 3*Bc*).

The quiescent state persisted until Na$^+$ extrusion deactivated I_{pump}, causing the stable branch to vanish via another SNIC and the family of periodic orbits to once again become globally attracting (a return to Fig. 3*Ba*). The resulting return to low rate spiking initiated a new burst cycle. The rhythm with I_{pump} was robust to variations in critical parameters (Fig. S2).

The Ca^{2+} and Na$^+$ dynamics during the burst cycle can be examined in the Ca^{2+}-Na$^+$ plane. For each fixed Na$^+$ greater than ≈5.1 mM, the branch of quiescent states extends over a range of Ca^{2+}, terminating when Ca^{2+} reaches an upper bound defined by the vertical portion of the SNIC bifurcation curve (Fig. 3*D*). During the burst, Na$^+$ levels exceed 5.1 mM, and thus the quiescent state exists for low Ca^{2+}. However, the burst terminates only when the Ca^{2+} decrease that follows depolarization block causes the trajectory to cross the SNIC curve (Fig. 3*D*, green). Likewise, burst initiation occurs only when a decline in Na$^+$ pushes the trajectory

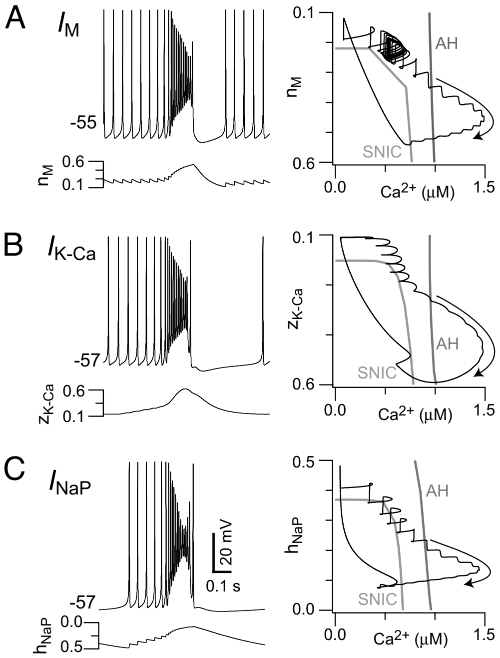

Fig. 4. Self-coupled model with different outward currents. Voltage (*Left*) and state-space trajectories with SNIC and AH curves (*Right*) are shown for M-like K^+ current (I_M), where n_M is the gating variable in n_M-Ca^{2+} state space (*A*); Ca^{2+}-dependent K^+ current ($I_{K\text{-}Ca}$), where $z_{K\text{-}Ca}$ is the gating variable in $z_{K\text{-}Ca}$-Ca^{2+} state space (*B*); and persistent Na^+ current (I_{NaP}), where h_{NaP} is the gating variable in h_{NaP}-Ca^{2+} state space (*C*). In contrast to *A* and *B*, h_{NaP} values are shown increasing along the *y* axis (*Right*) so that all panels on the *Right* represent more net outward current in the downward direction.

back across the horizontal portion of the SNIC curve, out of the region in which the quiescent states exist (Fig. 3*D*, black-red). Within the burst the trajectory crosses the AH bifurcation curve twice, signifying the start and end of spike attenuation (Fig. 3*D*, blue-green). The AH curve is vertical in the Ca^{2+}-Na^+ plane because the Na^+ accumulated from I_{CAN} does not influence voltage-dependent spike attenuation, although the fast sodium current I_{Na} may participate.

Fig. 3 shows that to prevent repetitive bursts, outward current must create a branch of stable nodes during the burst. Stable nodes capture the trajectory after synaptic depression decreases the Ca^{2+}, providing a period of quiescence. We posited that other activity-dependent net outward currents could replace I_{pump} and subserve this role. We examined 3 candidates that represent different classes of ion channels: a slowly-activating voltage-dependent M-like K^+ current (I_M, Fig. 4*A* and Fig. S3*B*), a Ca^{2+}-dependent K^+ current ($I_{K\text{-}Ca}$, Fig. 4*B* and Fig. S3*C*), and a slowly-inactivating persistent Na^+ current (I_{NaP}, Fig. 4*C* and Fig. S3*D*). The resulting bursts exhibited similar voltage trajectories regardless of which current we included (Figs. 4 *Left* and Fig. S3 top traces) and similar flows of Ca^{2+} together with a second slow variable involved in gating the added outward current (Figs. 4 and Fig. S3, blue traces). In all cases, depolarization block and synaptic depression stopped Ca^{2+} influx; these events do not require the activity-dependent net outward current. For I_M, $I_{K\text{-}Ca}$, and I_{NaP}, the second slow component played the same role as Na^+ did for I_{pump} activation in Fig. 3 and Fig. S3*A*. Specifically, the gating variables n_M, $z_{K\text{-}Ca}$, and h_{NaP} (for I_M, $I_{K\text{-}Ca}$, and I_{NaP}) evolved during the burst to evoke net outward currents and thus create a branch of stable quiescent states at low Ca^{2+}. In all cases, the trajectory settled onto this stable branch as Ca^{2+} decreased during the burst. The quiescent state disappeared due to deactivation of the outward current (or deinactivation of the inward current I_{NaP}, Fig. 4*C*), which restarted recurrent excitation. Although a variety of activity-dependent net outward currents produce quiescent interburst intervals, their gating properties and kinetics contrastingly influence the frequency of the rhythm.

To investigate whether our analysis applied to large networks, we interconnected 200 heterogeneous model neurons. Each neuron had 5 random input connections and 5 random projections to other cells. The full network with I_{pump} generated a CPG-like rhythm (Fig. S4*A*). Many neurons discharged sporadically at low rates (5–10 Hz) preceding the active phase because of heterogeneous values of E_L. Recurrent excitation ensured that bursts were globally synchronous, followed by an I_{pump}-mediated after-hyperpolarization (AHP). The AHP was clearly reflected in the widespread lack of spiking after each burst (Fig. S4*A*, raster plot), in the voltage trajectory of a typical neuron, and in the average network voltage (Fig. S4*A*). New cycles began when Na^+ decayed, I_{pump} deactivated, and the Ca^{2+} level increased again, accompanied by spontaneous spiking. Therefore, the dynamics of the 200-cell network were analogous to the self-coupled neuron with I_{pump} in Fig. 3.

Rhythmic bursts also occurred in the 200-neuron network when I_{pump} was replaced by I_M, $I_{K\text{-}Ca}$, or I_{NaP} (Fig. S4 *B–D*). The resulting full-network rhythm was dynamically equivalent to the paired-cell and single self-coupled neuron simulations displayed in Figs. 3 and 4 and Fig. S3.

Discussion

Mechanism For Burst Oscillations in a Recurrently Connected Excitatory Network. Here, we demonstrate a viable group pacemaker model, in which a rhythm emerges from an interconnected network of glutamatergic neurons that do not exhibit intrinsic bursting, regardless of applied current levels. Spontaneous spiking engenders positive feedback via recurrent excitation. Glutamate causes postsynaptic depolarization via ionotropic AMPA receptors and acts at group I mGluRs, which collectively increase intracellular Ca^{2+} and evoke I_{CAN} (11). I_{CAN} produces the drive potential underlying the burst (12, 13), which is a 10–30 mV envelope of depolarization with concomitant increase in spike rate that reflects burst onset.

Ours is the first CPG model, to our knowledge, that depends on glutamatergic signaling to gate postsynaptic burst-generating ion channels. The intensity of I_{CAN} in our model causes depolarization block and corresponding spike attenuation (Fig. S5), which has been repeatedly observed in respiratory neurons in vitro (22, 23), in partially intact in situ preparations (24), and in vivo (25). As a potentially rhythmogenic feature, burst-related depolarization block has also been reported in settings as diverse as rat spinal cord oscillations in culture (26) and turtle locomotor rhythms (27). Moreover, because spiking, synaptic transmission, Ca^{2+} influx, and I_{CAN} activation are directly linked in our model, our analyses lead us to predict that a form of synaptic depression contributes to burst termination in the preBötC.

Bifurcation Mechanisms Underlying Rhythms in a Group Pacemaker. The rhythm generated by our self-coupled and paired-cell models in the absence of an activity-dependent outward current or lowered E_L (i.e., Figs. 1 and 2*A*) can be classified mathematically as elliptic bursting (28, 29). Elliptic bursting with depolarization block has been demonstrated in an excitatory self-coupled model (30). In that model, the decay of synaptic excitation after burst termination alleviates depolarization block, allowing spiking to resume and starting the next burst cycle. By contrast, synaptic currents in our model contribute to the onset of depolarization block, but the blocked state can be maintained even if synaptic currents decay to negligible levels; the decay of Ca^{2+} allows spiking to resume.

Incorporating an activity-dependent outward current (I_{pump}, I_M, $I_{K\text{-}Ca}$, or I_{NaP} inactivation) can dramatically change the V-Ca^{2+} bifurcation diagram to include a stable branch of nodes (and a branch of saddle points) at low Ca^{2+}, which coalesces with the stable family of periodic orbits in a SNIC bifurcation at $(Ca^{2+})_{SNIC}$

$< (Ca^{2+})_{AH}$ (Fig. 3*B*). The resulting dynamics relies on 2 slow variables (e.g., Na^+ and Ca^{2+} in Fig. 3) and features 2 crossings of a curve of SNIC bifurcations in the V-Ca^{2+} bifurcation diagram, consistent with parabolic bursting (28, 29, 31). Noise fluctuations could also cause 2 crossings of the SNIC curve with low E_L. In its entirety, the model dynamics is in fact a hybrid of parabolic and elliptic bursting. The active phase begins by passage through a SNIC bifurcation with long initial interspike intervals, as in parabolic bursting, but subsequent I_{CAN}-mediated depolarization and spike attenuation are characteristic of elliptic bursting. Spike attenuation induces a decay of Ca^{2+} essential for burst termination via the recrossing of the SNIC curve. This more complex activity pattern has not, to our knowledge, been described in any previous model of cell or network burst oscillations.

Burst Initiation in a Group Pacemaker. We have shown that spontaneous spiking in some constituent neurons is essential to activate I_{CAN} and initiate bursts. This spiking can come from neurons that are tonically active (Fig. 1*A*) or via spontaneous fluctuations in silent neurons that spike occasionally when noise is included (Fig. 2*C*). Tonic neurons and quiescent neurons subject to noise-driven fluctuations provide qualitatively similar kindling for positive feedback in the form of temporal summation of EPSPs that leads to spiking, followed rapidly by I_{CAN} activation and burst onset. Tonic and noise-driven firing (Fig. S5*B*), and temporal summation of EPSPs (Fig. S5*C*), are observed in preBötC neurons. The rate of positive feedback may be influenced by properties not explicitly considered in this model such as K-ATP channels, transient K^+ currents, or hyperpolarization-activated cationic current (I_h) (see *SI Appendix*). These factors will impact burst frequency, but not necessarily influence the evolution of the burst as understood via the bifurcation structure in our model.

Burst Termination in a Group Pacemaker. Because I_{CAN} underlies the drive potential, bursts end when Ca^{2+} stops increasing and its decay deactivates I_{CAN}. If unchecked, Ca^{2+} accumulation via recurrent excitation allows for full network-wide I_{CAN} activation, locking the network in a state of active spiking or depolarization block. At least 3 mechanisms can halt Ca^{2+} build-up during a burst.

First, the loss of spiking from depolarization block may limit recurrent excitation. This is a form of short-term synaptic depression that would reduce Ca^{2+} entry through a variety of possible mechanisms (32–34). Depolarization block during the inspiratory burst is a widespread feature observed in medullary neurons (22–25) that has not, until now, been analyzed from a functional standpoint. Synaptic depression, driven by depolarization block, could contribute to the characteristically abrupt transition from inspiratory burst to expiratory interval.

Second, activating net outward currents could impede Ca^{2+} entry via hyperpolarization. Our analysis shows numerous ionic mechanisms for evoking outward currents, each of which becomes dominant after depolarization block (e.g., Figs. 3 and 4 and Figs. S3 and S4). Na/K ATPase pumps are particularly well suited for this role in the model because I_{CAN} drives Na^+ influx.

Finally, Ca^{2+} store receptors may desensitize or the stores may become depleted, which could lead to Ca^{2+} clearance and thus deactivate I_{CAN}. A burst-terminating role for receptor desensitization on intracellular Ca^{2+} stores has been hypothesized based on cultured preBötC neuron experiments and ring-oscillator models (12).

Burst termination in different group pacemakers could depend on any one of these mechanisms or a mix of all of them. Broadly speaking, it has been far easier in oscillatory cells and networks to experimentally identify the burst-generating mechanisms compared with burst-terminating mechanisms (20, 21), which suggests that multiple, coactive burst termination mechanisms may be common.

A Group Pacemaker May Explain the Neural Origins of Respiratory Rhythm. CPGs in a wide variety of animals, from mollusks to mammals, depend on reciprocal synaptic inhibition or specialized subpopulations of pacemaker neurons as the key building block of rhythmogenesis. However, respiratory oscillations in the preBötC cannot be attributed to either canonical mechanism. Emergent network oscillations, in which recurrent excitation provides gradual population-wide recruitment followed by activation of outward burst-terminating currents, have been proposed as a general alternative (3). Preliminary efforts to apply this idea to the preBötC were prescient (10) but were not formalized into a mechanistic model. At present, explicit models predominantly depend on the build-up of synaptic drive (35) and are inconsistent with the robust inspiratory bursts that are now known to rely on intrinsic features such as I_{CAN} (11–13).

I_{NaP} is universally expressed in the preBötC (36, 37), in CPGs (3, 38–40), and indeed in all central neurons (41). I_{NaP} was hypothesized to contribute to respiratory rhythm generation because it can give rise to intrinsic bursting-pacemaker properties. Butera *et al.* developed a seminal model that investigated the role of I_{NaP} in respiratory rhythm generation, which showed that individual I_{NaP}-expressing neurons could initiate, maintain and terminate bursts (42, 43). Despite the possible influence of I_{NaP} on single-cell dynamics, recent reports show that inspiratory rhythms persist under I_{NaP} blockade and, in the context of network activity, I_{NaP} plays little role in drive-potential generation (8, 9, 44–46) but see (47). Therefore, we generally study our model without I_{NaP} to focus on the plausibility of synaptically evoked I_{CAN} and the group pacemaker as a distinct rhythmogenic mechanism.

Here, we have shown that I_{NaP}, even when present at levels insufficient to generate bursts in isolated neurons, can contribute to burst termination and subsequent refractoriness (Fig. 4*C* and Fig. S3*D* and S4*D*). Prior models (42, 43, 48–50) with I_{NaP} showed that strong AMPA receptor-mediated interactions can cause network burst oscillations in the absence of intrinsic pacemaker properties. This mechanism, classified as a network oscillator by Grillner (3), differs from the group pacemaker because AMPA receptors act as charge carriers rather than catalysts for I_{CAN} activation as in our model.

Breathing patterns result from embedding the preBötC kernel in a larger respiratory network consisting of inhibitory populations in the rostral medulla and the pons (4). I_{NaP} has been reported to play a significant role in the embedded system, and becomes particularly important under certain physiological states such as gasping (44, 51). An open question is to what extent a CPG model, and the specific roles of I_{NaP} and I_{CAN}, influence the resulting motor pattern when the kernel is embedded in this more extensive network.

Implications for Central Pattern Generation. Efforts to understand CPGs typically focus on abstracting the essential rhythmogenic components. Here, we present a viable group pacemaker mechanism where the basic rhythmogenic unit is the synaptic gating of a cellular burst-generating conductance (I_{CAN}), coupled to any one of a host of feedback processes that check recurrent excitation. CPGs featuring this burst mechanism would likely exhibit certain properties not arising from more conventional network oscillator models in which recurrent excitation alone recruits network activity. First, recruiting I_{CAN} amplifies synaptic excitation, implying that once an activity threshold is reached, an abrupt and robust onset of network-wide activity would naturally occur in a group pacemaker (Fig. S4). Such a transition stands in contrast to the saw tooth-like rise in activity, or the bursts with spike frequencies similar to tonic spiking states, which are predicted patterns of activity for recurrent excitatory network oscillator models lacking synaptic gating of an intrinsic inward current. The resulting clarity of phase demarcation in a group pacemaker could prove advantageous for rhythms whose output is muscle contraction. Second, the transition to depolarization block provides an intrinsic mechanism to curtail the positive feedback component of the burst. In terms of breathing, this mechanism could provide a sensory-independent safeguard against apneusis or excessive lung inflation.

Even in CPGs that depend on synaptic inhibition or pacemaker properties, we postulate that incorporating a synaptically activated burst-generating conductance could contribute to enhancing the robustness or influencing the duration of the active phase. If so, such a conductance would be an advantageous target for neuromodulation because its contribution could be modified in response to behavioral imperatives or physiological challenges to alter active phase properties of the pattern and thus change the motor behavior, without jeopardizing the essential underlying rhythm.

Methods

Each neuron was modeled with a current-balance equation, in a simplified framework that makes bifurcation analysis tractable while still capturing the underlying biophysical phenomena (see *SI Appendix*). We simulated a coupled pair of neurons and a self-coupled neuron. In the 2-cell case, the cells' parameter values were identical except that the leak reversal potential E_L was varied to introduce heterogeneity. We used XPPAUT software for bifurcation analyses and numerical integration with an adjustable time step, 4th-order Runge-Kutta (RK4) method. XPPAUT is freely available for download from G. Bard Ermentrout, Ph.D., Department of Mathematics, The University of Pittsburgh, www.pitt.edu/~phase/.

Network simulations with 200 interconnected neurons were performed with custom software in C/C++ on Mac OS 10.4, using RK4 with a fixed time step of 0.1 ms. Unix-compatible source code for performing high-speed simulations with arbitrary network topology can be found at http://people.wm.edu/~cadeln/code.htm. The baseline parameter values were also used in the large network simulations, except for synaptic conductance and a Ca^{2+} flux scaling factor, which were decreased proportional to the number of synaptic inputs per neuron.

ACKNOWLEDGMENTS. This work was supported by National Science Foundation Grants DMS-0716936 and IOB-0616099 and the science education and research program at The College of William and Mary, which is funded by the Howard Hughes Medical Institute.

1. Gosgnach S, *et al.* (2006) V1 spinal neurons regulate the speed of vertebrate locomotor outputs. *Nature* 440:215–219.
2. Marder E (2001) Moving rhythms. *Nature* 410:755.
3. Grillner S (2006) Biological pattern generation: The cellular and computational logic of networks in motion. *Neuron* 52:751–766.
4. Feldman JL, Del Negro CA (2006) Looking for inspiration: New perspectives on respiratory rhythm. *Nat Rev Neurosci* 7:232–242.
5. Smith JC, Ellenberger HH, Ballanyi K, Richter DW, Feldman JL (1991) Pre-Bötzinger complex: A brainstem region that may generate respiratory rhythm in mammals. *Science* 254:726–729.
6. Brockhaus J, Ballanyi K (1998) Synaptic inhibition in the isolated respiratory network of neonatal rats. *Eur J Neurosci* 10:3823–3839.
7. Feldman JL, Smith JC (1989) Cellular mechanisms underlying modulation of breathing pattern in mammals. *Ann N Y Acad Sci* 563:114–130.
8. Del Negro CA, Morgado-Valle C, Feldman JL (2002) Respiratory rhythm: An emergent network property? *Neuron* 34:821–830.
9. Del Negro CA, *et al.* (2005) Sodium and calcium current-mediated pacemaker neurons and respiratory rhythm generation. *J Neurosci* 25:446–453.
10. Rekling JC, Feldman JL (1998) PreBötzinger complex and pacemaker neurons: Hypothesized site and kernel for respiratory rhythm generation. *Annu Rev Physiol* 60:385–405.
11. Pace RW, Del Negro CA (2008) AMPA and metabotropic glutamate receptors cooperatively generate inspiratory-like depolarization in mouse respiratory neurons in vitro. *Eur J Neurosci* 28:2434–2442.
12. Mironov SL (2008) Metabotropic glutamate receptors activate dendritic calcium waves and TRPM channels which drive rhythmic respiratory patterns in mice. *J Physiol* 586:2277–2291.
13. Pace RW, Mackay DD, Feldman JL, Del Negro CA (2007) Inspiratory bursts in the preBötzinger Complex depend on a calcium-activated nonspecific cationic current linked to glutamate receptors. *J Physiol* 582(Pt 1):113–125.
14. Wang D, Grillner S, Wallen P (2006) Effects of flufenamic acid on fictive locomotion, plateau potentials, calcium channels and NMDA receptors in the lamprey spinal cord. *Neuropharmacology* 51:1038–1046.
15. Rekling JC, Feldman JL (1997) Calcium-dependent plateau potentials in rostral ambiguus neurons in the newborn mouse brain stem in vitro. *J Neurophysiol* 78:2483–2492.
16. Zhu ZT, Munhall A, Shen KZ, Johnson SW (2004) Calcium-dependent subthreshold oscillations determine bursting activity induced by N-methyl-D-aspartate in rat subthalamic neurons in vitro. *Eur J Neurosci* 19:1296–1304.
17. Fransen E, Tahvildari B, Egorov AV, Hasselmo ME, Alonso AA (2006) Mechanism of graded persistent cellular activity of entorhinal cortex layer v neurons. *Neuron* 49:735–746.
18. Angstadt JD, Friesen WO (1991) Synchronized oscillatory activity in leech neurons induced by calcium channel blockers. *J Neurophysiol* 66:1858–1873.
19. Johnson SW, Seutin V, North RA (1992) Burst firing in dopamine neurons induced by N-methyl-D-aspartate: Role of electrogenic sodium pump. *Science* 258:665–667.
20. Ballerini L, Bracci E, Nistri A (1997) Pharmacological block of the electrogenic sodium pump disrupts rhythmic bursting induced by strychnine and bicuculline in the neonatal rat spinal cord. *J Neurophysiol* 77:17–23.
21. Darbon P, Tscherter A, Yvon C, Streit J (2003) Role of the electrogenic Na/K pump in disinhibition-induced bursting in cultured spinal networks. *J Neurophysiol* 90:3119–3129.
22. Rekling JC, Champagnat J, Denavit-Saubie M (1996) Electroresponsive properties and membrane potential trajectories of three types of inspiratory neurons in the newborn mouse brain stem in vitro. *J Neurophysiol* 75:795–810.
23. Onimaru H, Arata A, Homma I (1997) Neuronal mechanisms of respiratory rhythm generation: An approach using in vitro preparation. *Jpn J Physiol* 47:385–403.
24. Paton JF (1997) Rhythmic bursting of pre- and post-inspiratory neurones during central apnoea in mature mice. *J Physiol* 502 (Pt 3):623–639.
25. Schwarzacher SW, Wilhelm Z, Anders K, Richter DW (1991) The medullary respiratory network in the rat. *J Physiol* 435:631–644.
26. Yvon C, Czarnecki A, Streit J (2007) Riluzole-induced oscillations in spinal networks. *J Neurophysiol* 97:3607–3620.
27. Berkowitz A (2008) Physiology and morphology of shared and specialized spinal interneurons for locomotion and scratching. *J Neurophysiol* 99:2887–2901.
28. Bertram R, Butte MJ, Kiemel T, Sherman A (1995) Topological and phenomenological classification of bursting oscillations. *Bull Math Biol* 57:413–439.
29. Rinzel J (1987) A formal classification of bursting mechanisms in excitable systems. *Proceedings of the International Congress of Mathematicians*, ed Gleason A (American Mathematical Society), pp 1578–1594.
30. Ermentrout B, Dutta-Moscato J, Pinto D (2005) in *Bursting: The genesis of rhythm in the nervous system*, eds Coombes S, Bressloff PC (World Scientific, Hackensack, NJ), pp 385–396.
31. Ermentrout GB, Kopell N (1986) Parabolic Bursting in an Excitable System Coupled with a Slow Oscillation. *SIAM J Appl Math* 46:233–253.
32. Brody DL, Yue DT (2000) Release-independent short-term synaptic depression in cultured hippocampal neurons. *J Neurosci* 20:2480–2494.
33. Dobrunz LE, Huang EP, Stevens CF (1997) Very short-term plasticity in hippocampal synapses. *Proc Natl Acad Sci USA* 94:14843–14847.
34. Forsythe ID, Tsujimoto T, Barnes-Davies M, Cuttle MF, Takahashi T (1998) Inactivation of presynaptic calcium current contributes to synaptic depression at a fast central synapse. *Neuron* 20:797–807.
35. Kosmidis EK, Pierrefiche O, Vibert JF (2004) Respiratory-like rhythmic activity can be produced by an excitatory network of non-pacemaker neuron models. *J Neurophysiol* 92:686–699.
36. Del Negro CA, Koshiya N, Butera RJ, Jr, Smith JC (2002) Persistent sodium current, membrane properties and bursting behavior of pre-Bötzinger complex inspiratory neurons in vitro. *J Neurophysiol* 88:2242–2250.
37. Ptak K, *et al.* (2005) Sodium currents in medullary neurons isolated from the pre-Bötzinger complex region. *J Neurosci* 25:5159–5170.
38. Darbon P, Yvon C, Legrand JC, Streit J (2004) INaP underlies intrinsic spiking and rhythm generation in networks of cultured rat spinal cord neurons. *Eur J Neurosci* 20:976–988.
39. Tazerart S, Viemari JC, Darbon P, Vinay L, Brocard F (2007) Contribution of persistent sodium current to locomotor pattern generation in neonatal rats. *J Neurophysiol* 98:613–628.
40. Zhong G, Masino MA, Harris-Warrick RM (2007) Persistent sodium currents participate in fictive locomotion generation in neonatal mouse spinal cord. *J Neurosci* 27:4507–4518.
41. Bean BP (2007) The action potential in mammalian central neurons. *Nat Rev Neurosci* 8:451–465.
42. Butera RJ, Jr, Rinzel J, Smith JC (1999) Models of respiratory rhythm generation in the pre-Bötzinger complex. I. Bursting pacemaker neurons. *J Neurophysiol* 82:382–397.
43. Butera RJ, Jr, Rinzel J, Smith JC (1999) Models of respiratory rhythm generation in the pre-Bötzinger complex. II. Populations Of coupled pacemaker neurons. *J Neurophysiol* 82:398–415.
44. Paton JF, Abdala AP, Koizumi H, Smith JC, St-John WM (2006) Respiratory rhythm generation during gasping depends on persistent sodium current. *Nat Neurosci* 9:311–313.
45. Pena F, Parkis MA, Tryba AK, Ramirez JM (2004) Differential Contribution of Pacemaker Properties to the Generation of Respiratory Rhythms during Normoxia and Hypoxia. *Neuron* 43:105–117.
46. Pace RW, Mackay DD, Feldman JL, Del Negro CA (2007) Role of persistent sodium current in mouse preBötzinger Complex neurons and respiratory rhythm generation. *The J Physiol* 580(Pt 2):485–496.
47. Koizumi H, Smith JC (2008) Persistent Na^+ and K^+-dominated leak currents contribute to respiratory rhythm generation in the pre-Bötzinger complex in vitro. *J Neurosci* 28:1773–1785.
48. Rubin J (2006) Bursting induced by excitatory synaptic coupling in nonidentical conditional relaxation oscillators or square-wave bursters. *Phys Rev E* 74:1–15.
49. Best J, Borisyuk A, Rubin J, Terman D, Wechselberger M (2005) The dynamic range of bursting in a model respiratory pacemaker network. *SIAM J App Dyn Sys* 4:1107–1139.
50. Purvis LK, Smith JC, Koizumi H, Butera RJ (2007) Intrinsic bursters increase the robustness of rhythm generation in an excitatory network. *J Neurophysiol* 97:1515–1526.
51. Smith JC, Abdala AP, Koizumi H, Rybak IA, Paton JF (2007) Spatial and functional architecture of the mammalian brain stem respiratory network: A hierarchy of three oscillatory mechanisms. *J Neurophysiol* 98:3370–3387.